

XAS analysis of iron and palladium bonded to a polysaccharide produced anaerobically by a strain of *Klebsiella oxytoca*

Iztok Arčon,^{a,b,*} Stefano Paganelli,^c Oreste Piccolo,^{c,d} Michele Gallo,^c Katarina Vogel-Mikuš^e and Franco Baldi^c

Received 17 March 2015

Accepted 29 May 2015

Edited by R. W. Strange, University of Liverpool, UK

Keywords: citrate fermentation; bi-metallic exopolysaccharide; Fe K-edge; Pd K-edge; XANES; EXAFS; μ -XRF.

Supporting information: this article has supporting information at journals.iucr.org/s

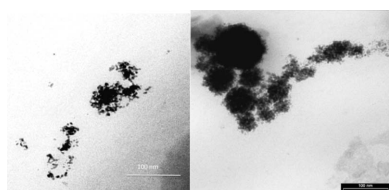
^aUniversity of Nova Gorica, Vipavska 13, Nova Gorica 5000, Slovenia, ^bInstitut Jozef Stefan, Jamova 39, Ljubljana 1000, Slovenia, ^cDipartimento di Scienze Molecolari e Nanosistemi, Università Cà Foscari, Via Torino 155, 30170 Venezia-Mestre, Italy, ^dSCSOP, Via Bornò 5, Sirtori 23896, Italy, and ^eDepartment of Biology, Biotechnical Faculty, University of Ljubljana, Večna pot 111, Ljubljana 1000, Slovenia. *Correspondence e-mail: iztok.arcon@ung.si

Klebsiella oxytoca BAS-10 ferments citrate to acetic acid and CO₂, and secretes a specific exopolysaccharide (EPS), which is able to bind different metallic species. These biomaterials may be used for different biotechnological purposes, including applications as innovative green biogenerated catalysts. In production of biogenerated Pd species, the Fe(III) as ferric citrate is added to anaerobic culture of *K. oxytoca* BAS-10, in the presence of palladium species, to increase the EPS secretion and improve Pd-EPS yield. In this process, bi-metallic (FePd-EPS) biomaterials were produced for the first time. The morphology of bi-metallic EPS, and the chemical state of the two metals in the FePd-EPS, are investigated by transmission electron microscopy, Fourier transform infra-red spectroscopy, micro-X-ray fluorescence, and X-ray absorption spectroscopy methods (XANES and EXAFS), and compared with mono-metallic Pd-EPS and Fe-EPS complexes. Iron in FePd-EPS is in the mineralized form of iron oxides/hydroxides, predominantly in the form of Fe³⁺, with a small amount of Fe²⁺ in the structure, most probably a mixture of different nano-crystalline iron oxides and hydroxides, as in mono-metallic Fe-EPS. Palladium is found as Pd(0) in the form of metallic nanoparticles with face-centred cubic structure in both bi-metallic (FePd-EPS) and mono-metallic (Pd-EPS) species. In bi-metallic species, Pd and Fe nanoparticles agglomerate in larger clusters, but they remain spatially separated. The catalytic ability of bi-metallic species (FePd-EPS) in a hydro-dechlorination reaction is improved in comparison with mono-metallic Pd-EPS.

1. Introduction

Bio-generated polymeric substances, such as polysaccharides, are able to bind metals and consequently protect cells from environmental stress (Deschatre *et al.*, 2013; Shuhong *et al.*, 2014). This strategy was also found in *Klebsiella oxytoca* strain BAS-10, isolated from an acid drainage mining area enriched with toxic metals (Baldi *et al.*, 2001).

The strain can ferment Fe(III)-citrate under anaerobic conditions, in addition to the usual Na-citrate, as the sole energy and organic carbon source to acetic acid and CO₂ (Gallo *et al.*, 2012) producing, during the stationary phase, a specific exopolysaccharide (EPS), constituted by a branched heptasaccharide repeating unit, which strongly binds Fe(III) (Leone *et al.*, 2007), as has been demonstrated by cyclic voltammetric measurements (Baldi *et al.*, 2009). Recently BAS-10 was used as a micro-factory to produce different types of Me-EPS species (Me = Fe, Pd, Ag), which have shown useful properties (Baldi *et al.*, 2011; Paganelli *et al.*, 2013; Battistel *et al.*, 2015). The yield of different Me-EPS species depended strongly on the type of the metal, and on the source



© 2015 International Union of Crystallography

of metal, *i.e.* metal salt, added to the growing culture of BAS-10. The highest yield of Me-EPS was found when Fe(III)-citrate was used as sole energy and carbon source. With additions of other metals, where the carbon and energy source was Na-citrate, the yield was often very low due to the inhibition effect of the added metals.

In order to produce a higher amount of Pd-EPS it was necessary to protect cells from palladium toxicity. For this purpose two different amounts of Fe(III)-citrate were added to Na-citrate in the medium. We expected that PdNO₃ in the stationary phase might induce a production of EPS, which would embed the two metals (Fe and Pd) in the following chemical states: Fe(II), Fe(III), Pd(II) and Pd(0). These new bi-metallic products (FePd-EPS) and, for comparison, mono-metallic Pd-EPS were characterized by X-ray absorption spectroscopy methods XANES (X-ray absorption near-edge structure) and EXAFS (extended X-ray absorption fine structure) to obtain structural information about iron and palladium in (FePd-EPS) complexes at the atomic scale (Ravel & Newville, 2005; Arčon *et al.*, 2012). With Fe and Pd *K*-edge XANES the valence state of iron and palladium in the sample and the local symmetry of their unoccupied orbitals can be deduced from the shape and energy shift of the Fe and Pd *K*-absorption edge (Arčon *et al.*, 2007, 2012; Wong *et al.*, 1984; Kuezman *et al.*, 2009; Dominko *et al.*, 2010). In Fe and Pd *K*-edge EXAFS analysis the number and species of neighbor atoms around Fe and Pd, their distance from the Fe or Pd atom, and the thermal or structural disorder of their positions are determined (Arčon *et al.*, 2005, 2012; Wong *et al.*, 1984; Kuezman *et al.*, 2009; Dominko *et al.*, 2010; Rehr *et al.*, 1992; Coe *et al.*, 1995). In addition, synchrotron-radiation-based micro-X-ray fluorescence (SR μ -XRF) (Koren *et al.*, 2013) was used to map distributions of Fe, Pd and P elements at the micrometer-size level in the bi-metallic FePd-EPS samples. Finally we evaluated the influence of the presence of iron on the catalytic activity of palladium species in these mono- or bi-metallic EPS samples, in the hydrodechlorination of 1,2,4-trichlorobenzene.

2. Materials and methods

2.1. General

NaHCO₃, NH₄Cl, MgSO₄·H₂O, NaH₂PO₄, KCl, Na-citrate, Fe(III)-citrate, Pd(NO₃)₂ and 1,2,4-trichlorobenzene were Aldrich products. Gas chromatography (GC) analyses were carried out on an Agilent 6850A gas chromatograph (HP1 column 30 m × 0.32 mm × 0.25 μ m) and gas chromatography–mass spectrometry (GC–MS) analyses were performed by an Agilent MS Network 5937 (HP-5MS column 30 m × 0.25 mm × 0.25 μ m). IR spectra (KBr pellets) were recorded on an FTIR Nicolet Magna 750 instrument. Solvents were purified as described in the literature (Perrin & Armarego, 1988).

2.2. Metal polysaccharides production and purification

The *Klebsiella oxytoca* strain BAS-10 was retrieved from cryovials kept at 193 K in 25% glycerol in Nutrient broth

(Difco). An aliquot of 1 ml of overnight culture was transferred under anaerobic conditions in three different media: the NaC, the FeNaC₂ and FeNaC₁₀. The NaC medium contained, per liter, 2.5 g NaHCO₃, 1.5 g NH₄Cl, 1.5 g MgSO₄·H₂O, 0.6 g NaH₂PO₄, 0.1 g KCl and 14.7 g Na-citrate. The FeNaC₂ medium, as carbon and energy source, contained 14.3 g Na-citrate and 0.235 g Fe(III)-citrate. The FeNaC₁₀ medium contained 13.23 g Na-citrate and 1.315 g Fe(III)-citrate. All three media were buffered at pH 7.6 with NaOH. The cultivation of strain BAS-10 was performed in 1 L of medium incubating at 303 K under anaerobic conditions. When a cell density (~ 1.0 Abs_{600nm}) was reached in the three media, each culture was amended with 50 mg of total Pd as Pd(NO₃)₂. The anaerobic conditions were maintained by fluxing N₂ until the culture and the pirez-bottles were sealed again and incubated for a further seven days. All cultures were first centrifuged to eliminate bacterial cells. The supernatants were treated with 800 ml of cooled ethyl alcohol (95%) to precipitate the metal polysaccharides. The purifications were repeated twice. Each colloidal material was finally dried out under vacuum and grinded to powder to obtain three different materials: Pd-EPS, FePd-EPS(A) and FePd-EPS(B). Summarizing, the Pd-EPS was produced by adding only 50 mg Pd_{tot} whereas the FePd-EPS(A) was produced by adding 50 mg Pd_{tot} plus 50 mg Fe_{tot} as Fe(III)-citrate, and the FePd-EPS(B) was produced by adding 50 mg Pd_{tot} plus 280 mg Fe_{tot} as Fe(III)-citrate.

2.3. Element determination in polysaccharides

The total amounts of Fe, Pd and P were determined in 1 mg of pulverized FePd-EPS(A), FePd-EPS(B) and Pd-EPS. The samples were digested with 2 ml of aqua regia and heated at 333 K until a solution was obtained. The total amounts of elements were determined *versus* their relative standards solutions by inductively coupled plasma atomic emission spectrometry (ICP-AES) (Optima 3100, Perkin Elmer) (Rigo *et al.*, 2009).

2.4. Transmission electron microscopy

Morphological differences of metal polysaccharides were observed with transmission electron microscopy (TEM). An aliquot of 10 mg of each compound was re-suspended in 1 ml milliQ, and previously treated for 10 min in an ultrasonic bath; 10 μ L of suspension was mounted on a platinum grid treated with Formvar resin biofilm to determine the fine structure. The liquid was evaporated at room temperature and the sample was observed with a Jeol JEM 100b microscope operating under standard conditions (Paganelli *et al.*, 2013).

2.5. XAFS analysis

Three samples [Pd-EPS, FePd-EPS(A) and FePd-EPS(B)] were prepared in the form of homogeneous self-standing pellets with the total absorption thickness (μ d) of about 1.5 above the investigated Fe *K*-edge (7112 eV) and Pd *K*-edge (24350 eV). Fe *K*-edge absorption spectra were measured at room temperature in transmission detection mode at the

XAFS beamline of the ELETTRA synchrotron radiation facility in Trieste, Italy. A Si (111) double-crystal monochromator was used with 0.8 eV resolution at 7 keV. Higher-order harmonics were effectively eliminated by detuning the monochromator crystals to 60% of the rocking curve maximum. The intensity of the monochromatic X-ray beam was measured by three consecutive 30 cm-long ionization detectors filled, respectively, with the following gas mixtures: 580 mbar N₂ and 1420 mbar He; 1000 mbar N₂, 90 mbar Ar and 910 mbar He; 350 mbar Ar, 1000 mbar N₂ and 650 mbar He. In the XANES region equidistant energy steps of 0.25 eV were used, while for the EXAFS region equidistant k steps of 0.03 Å⁻¹ were adopted with an integration time of 1 s per step. The exact energy calibration was established with simultaneous absorption measurement on a 5 µm-thick Fe metal foil placed between the second and the third ionization chamber. Absolute energy reproducibility of the measured spectra was ±0.03 eV. Pd K -edge spectra were measured in transmission mode at beamline C of HASYLAB at DESY in Hamburg, Germany. The beamline was equipped with a Si 311 two-crystal monochromator with about 2 eV resolution at the Pd K -edge. Higher harmonics were eliminated by detuning the monochromator crystals to 60% of the rocking curve maximum, using the beam-stabilization feedback control. The intensity of the monochromated beam was monitored with three 10 cm-long ionization detectors filled with krypton, the first to a pressure of 190 mbar, and the second and third to a pressure of 1000 mbar. The samples were placed between the first pair of detectors, with the reference Pd metal foil between the last pair, to check the stability of the energy scale. The absorption spectra were measured within the interval [−250 eV to 1000 eV] relative to the Pd K -edge. In the XANES region, equidistant energy steps of 0.5 eV were used, while, for the EXAFS region, equidistant k -steps ($\Delta k = 0.03 \text{ \AA}^{-1}$) were adopted, with an integration time of 1 s per step.

2.6. Mapping of element distributions using synchrotron micro-X-ray fluorescence spectrometry

The mapping of the Fe, Pd and P element distributions in the FePd-EPS(A), FePd-EPS(B) sample pellets was performed using a scanning transmission X-ray microscope at the ID21 beamline of the European Synchrotron Radiation Facility, Grenoble, France. The X-ray beam delivered by the undulator was monochromated using a Si 111 double-crystal monochromator, and focused to a submicrometer probe (0.8 µm × 0.7 µm) by a zone plate. The fluorescence emission of the sample was collected using an 80 mm² XFlash 5100 silicon drift diode (Bruker, Germany). The excitation energy for the scan was set to 7300 eV (*i.e.* above the Fe K -edge), and the distribution maps of Fe, Pd and P were simultaneously recorded. In FePd-EPS(A) and FePd-EPS(B) sample pellets a region of 100 µm × 100 µm was chosen for the mapping with 100 × 100 pixels mesh using a video-microscope installed in an experimental chamber, and scanned with a micro-beam under vacuum, with a dwell time of 300 ms per pixel. The dead time of the measurements was below 5%. X-ray fluorescence

(XRF) spectra were recorded using an X-ray Instrumentation Associates acquisition system. In the quantification procedure, the recorded X-ray spectra were first deconvoluted using the *PyMca* software (Solé *et al.*, 2007), then corrected for dead time, and normalized per beam current in the ring (Koren *et al.*, 2013). Element intensities with their uncertainties were obtained in a matrix form, with data for each measured pixel in a single row. The quantification procedure applied was an extension of the quantification used in the conventional XRF analysis (Kump *et al.*, 2007), and was based on fundamental parameters. The fundamental parameters used were taken from the database of Elam *et al.* (2002) and the system of equations for measured elements was based on the relationship initially developed by Sherman (1955). The sample thickness was calculated from peak absorption of X-rays at 7300 eV, taking into account the absorption coefficient in carbohydrates at 7300 eV. The calibration of the XRF system was performed with a set of thin (a few tens of µg cm⁻² thick) standard samples (Cr, Mn, Fe) obtained from Micromatter, and the respective geometry and/or instrumental constants were calculated (He & Espen, 1991). Additionally, the geometric constant of the same value was also obtained from the measured incident photon beam by the photodiode placed behind the sample, and considering the solid angles extended from the sample to the detector. Using the fundamental parameters, the respective element sensitivities were then calculated. The uncertainties introduced by the fundamental parameters and the calibration procedure were partially compensated for, if the experimental sensitivities were used in further quantifications. The measurements were validated by scanning multi-element standard reference materials: NIST SRM 1573a, CRM 129 and OU-10 (Koren *et al.*, 2013).

2.7. Hydrodechlorination of 1,2,4-trichlorobenzene (1,2,4-TCB) experiments

A sample of Pd-EPS or FePd-EPS(A) or FePd-EPS(B) (the amount used, referred to palladium g atom content, is indicated in Table 4) was stirred in a Schlenk tube under nitrogen in 2 ml of distilled water for about 10 min. A solution of 259 mg (1.96 mmol) of 1,2,4-trichlorobenzene (1,2,4-TCB) in 1 ml of THF was then added to the aqueous phase. The Schlenk tube was then transferred into a 150 ml stainless steel autoclave under nitrogen, pressurized with 3 MPa of H₂ and stirred at 333 or 353 K for 20 h. The reactor was then cooled to room temperature and the residual gases released. Diethyl ether was added and the organic phase was separated, dried on Na₂SO₄ and analyzed by GC (flame ionization detector) and GC–MS. In some runs the catalyst was also recycled for a further experiment. In this case, the aqueous phase, containing the catalyst, was extracted three to five times with 3 ml portions of diethyl ether until 1,2,4-TCB, so that the hydrodechlorination products were no longer present in the organic extract (analyses carried out by GC and GC–MS), and then the aqueous extract was used in a recycling experiment.

Table 1

Yields and Fe and Pd concentrations in the three samples with and without iron additions.

	Pd-EPS	FePd-EPS(A)	FePd-EPS(B)
Yield (mg L ⁻¹)	178	450	1100
Fe (%)	0.033	7.4	14
Pd (%)	11	8.4	2.2

3. Results

3.1. Elemental analysis and TEM

The strain *K. oxytoca* BAS-10 produces, under anaerobic conditions, an EPS having a branched heptasaccharide repeating unit, the structure of which consists of four rhamnose (Rha), two glucuronic acids (GlcA) and one galactose (Gal) bound by α and β glycosidic bonds (Leone *et al.*, 2007; Baldi *et al.*, 2009) as shown in Fig. 1. EPS binds iron and other metals during the bacterial growth. To date, only mono-metallic EPS have been biosynthesized (Baldi *et al.*, 2010, 2011). In this study we produced for the first time two bi-metallic species FePd-EPS(A) and FePd-EPS(B) in order to obtain more biomaterials from the microbial cultures. Yields of FePd-EPS(A) (450 mg l⁻¹) and FePd-EPS(B) (1100 mg l⁻¹) were significantly higher than the yield of mono-metallic Pd-EPS obtained without iron addition (178 mg l⁻¹) (Table 1). Furthermore, the Pd incorporated in the EPS in the absence of iron was only 39% of the charged amount during the growth; the content of Pd present in FePd-EPS(A) and in FePd-EPS(B) instead corresponded to 76% and 48% of the charged metal, respectively. Also iron recovery in Me-EPS was higher when the weight of Fe and Pd salts was the same [67% in FePd-EPS(A) versus 55% in FePd-EPS(B)].

The TEM micrographs of Pd-EPS without iron additions and FePd-EPS(B) with the highest iron content (Fig. 2) show formation of electron-dense nano-particles in EPS with significant differences in particle size. In Pd-EPS the Pd nano-particles are agglomerated in small clusters (Fig. 2a). In the presence of iron, larger clusters of (FePd)-EPS are produced (Fig. 2b).

3.2. Fe and Pd K-edge XANES

The Fe and Pd K-edge XANES analysis was used to determine the average Fe and Pd valence state in FePd-EPS(A), FePd-EPS(B) and Pd-EPS samples. The analysis of XANES spectra was performed with the *IFEFFIT* program package *ATHENA* (Ravel & Newville, 2005). The relative K-shell contribution in the absorption spectra (Figs. 3 and 4) is obtained by the standard procedure (Ravel & Newville, 2005; Wong *et al.*, 1984) by removing the extrapolated best-fit linear

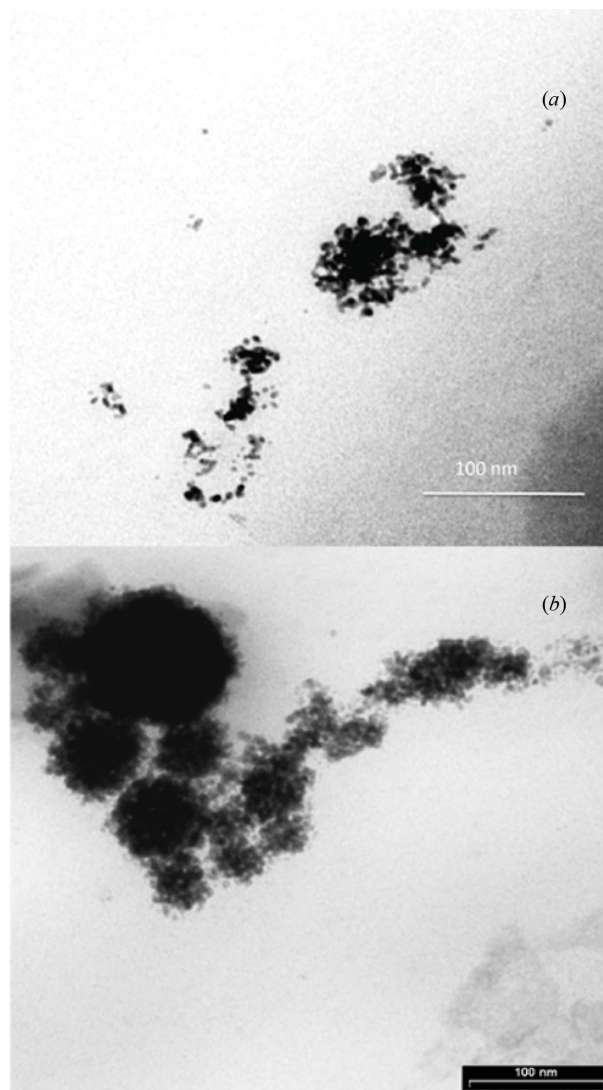


Figure 2

(a) TEM micrograph of a cell of *K. oxytoca* strain BAS-10 surrounded by electron-dense nanoparticles of Pd (bar = 100 nm). (b) TEM micrograph of FePd-EPS(B) extracted from bacterial culture with amorphous and ordered states nano-particles (bar = 100 nm).

function determined in the pre-edge region (-150 eV to -30 eV), and by conventional normalization, extrapolating the post-edge spline background, determined in the range from 100 to 900 eV, to set the Fe or Pd K-edge jump to 1. Different local environments of the cation result in different K-edge profiles and pre-edge lines in the XANES spectra. The energy position of the absorption edge and the pre-edge features are correlated with the valence state of the absorbing atom in the sample. With increasing oxidation state each absorption feature in the XANES spectrum is shifted to higher energies. Largest shifts, of the order of few eV per valence state, are observed for the energy position of the absorption edge (Wong *et al.*, 1984; Arçon *et al.*, 2007; Kuezma *et al.*, 2009; Dominko *et al.*, 2010). The Pd K-edge profiles of the FePd-EPS(A), FePd-

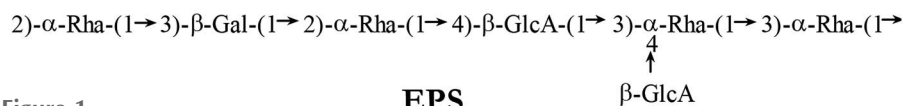


Figure 1

Exopolysaccharide (EPS).

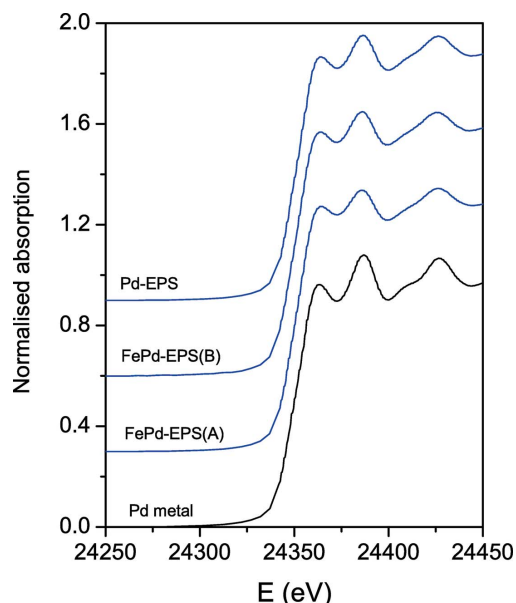


Figure 3
Pd *K*-edge XANES spectra of the FePd-EPS(A), FePd-EPS(B) and Pd-EPS samples and reference Pd metal foil with f.c.c. crystal structure.

EPS(B) and Pd-EPS samples (Fig. 3) are almost identical to the Pd XANES spectrum of the Pd metal foil with face-centered cubic (f.c.c.) crystalline structure, which clearly indicates that palladium in the samples is mainly in the form of Pd(0). The Fe *K*-edge profiles of the FePd-EPS(A) and FePd-EPS(B) samples (Fig. 4), which are very similar but not identical to one another, are similar in shape to that of the reference Fe-EPS sample (Arčon *et al.*, 2012), indicating that Fe in FePd-EPS samples has a similar local environment as was reported for the Fe-EPS sample or ferritine (Watt, 2011),

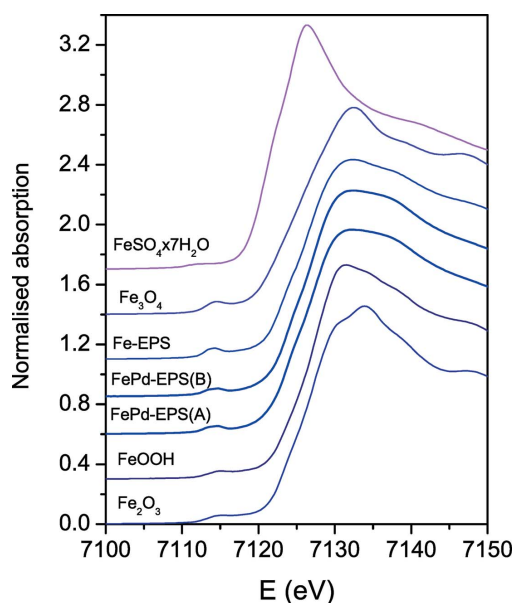


Figure 4
Fe *K*-edge XANES spectra of the FePd-EPS(A) and FePd-EPS(B) samples and reference iron compounds with octahedral iron coordination and different iron valence states between Fe²⁺ and Fe³⁺ (FeSO₄·7H₂O, α-FeOOH, Fe₂O₃ and Fe-EPS sample) (Arčon *et al.*, 2012).

i.e. a mixture of Fe-oxides and hydroxides. The average Fe valence state in the samples can be deduced from the energy position of the Fe *K*-edge. From the XANES spectra of the reference compounds FeSO₄·7H₂O, Fe₃O₄, α-FeOOH and Fe₂O₃ with known structure and Fe valence state, we found that the Fe *K*-edge shifts for about 4.5 eV per valence from Fe²⁺ to Fe³⁺. The energy position of the Fe *K*-edge in FePd-EPS samples is between the edge position of Fe³⁺ compounds and the edge position of the Fe-EPS compound, where the average valence state of iron was found to be 2.82⁺ (Arčon *et al.*, 2012), indicating that iron in the FePd-EPS samples is predominantly in the trivalent state with a small amount of Fe²⁺ in the mixture. If the sample contains a mixture of two or more compounds of the same cation with different local structure and valence state, the measured XANES spectrum is a linear combination of individual XANES spectra of the different cation sites. In such cases the relative amounts of the cation at each site and the average valence state of the cation in the sample can be determined by the linear combination fit with XANES spectra of proper reference compounds with known valence states of the element, with similar symmetry, same type of neighbor atoms in nearest coordination shells, arranged in a similar local structure (Arčon *et al.*, 2007, 2012; Kuezma *et al.*, 2009; Dominko *et al.*, 2010). The procedure is applied to Fe *K*-edge XANES spectra measured on FePd-EPS samples. The spectra can be best described by the linear combination of the XANES profiles of α-FeOOH, and Fe₂O₃ as a reference for Fe³⁺, and Fe-EPS as a reference for Fe^{2.82+} (Figs. 5 and 6). In this way we were able to determine that the average Fe valence state in the FePd-EPS(A) and FePd-EPS(B) samples is 2.89⁺ and 2.92⁺, respectively, with uncertainty of about 1%. The same result within 1% uncertainty is obtained if a linear combination fit is performed with two reference XANES profiles: α-FeOOH as a reference for Fe³⁺, and Fe₃O₄ as a reference for Fe^{2.67+}. The presence of a small part of divalent iron could be explained by the presence of nano-crystalline Fe₃O₄ particles with spinel structure, where divalent Fe cations occupy tetrahedral sites in the crystalline structure. Tetrahedrally coordinated Fe cations are indicated also by the characteristic shape of the pre-edge resonances. The Fe *K*-edge XANES results indicate that iron in FePd-EPS(A) and FePd-EPS(B) samples is a mixture of nano-crystalline iron oxides and hydroxides as in the case of Fe-EPS (Arčon *et al.*, 2012), but with different relative amounts.

3.3. Fe and Pd *K*-edge EXAFS

Fe and Pd *K*-edge EXAFS analysis is used to directly probe the local structure around Fe and Pd cations in the FePd-EPS samples. The quantitative analysis of Fe and Pd EXAFS spectra is performed with the *IFEFFIT* program package (Ravel & Newville, 2005). In the Fourier transform magnitude of the Fe *K*-edge EXAFS spectra of FePd-EPS(A) and FePd-EPS(B) samples, two distinct peaks are observed (Fig. 7), representing the contributions of photoelectron scattering on the nearest shells of neighbors around the Fe atom. A strong peak in the *R* range between 1 Å and 2.2 Å can be attributed

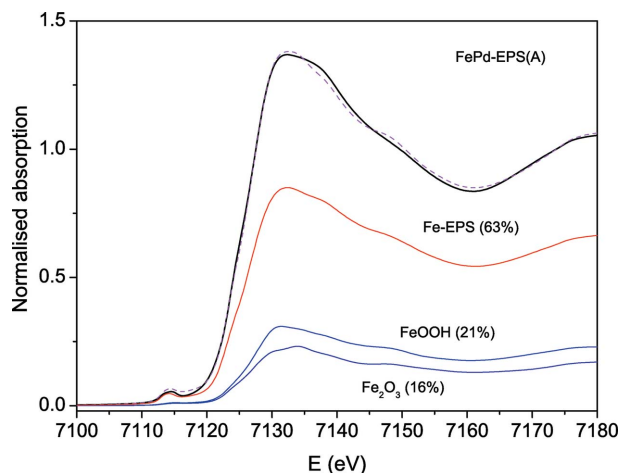


Figure 5 Fe *K*-edge XANES spectrum of the FePd-EPS(A) sample. Black solid line: experiment; magenta dashed line: best-fit linear combination of XANES profiles of Fe-EPS (63%), α -FeOOH (21%) and Fe_2O_3 (16%). Fit components are shown below.

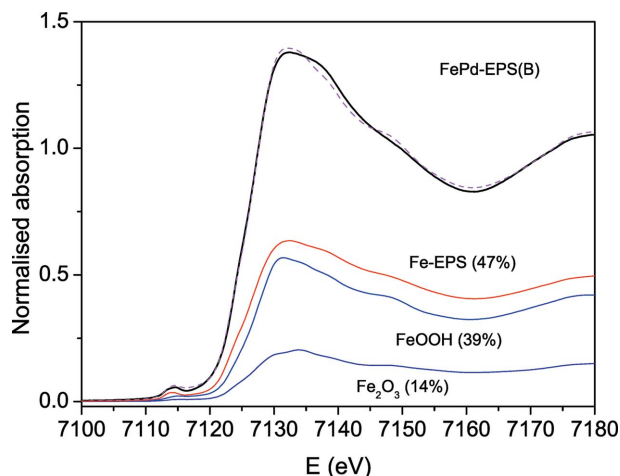


Figure 6 Fe *K*-edge XANES spectrum of the FePd-EPS(B) sample. Black solid line: experiment; magenta dashed line: best-fit linear combination of XANES profiles of Fe-EPS (47%), α -FeOOH (39%) and Fe_2O_3 (14%). Fit components are shown below.

to photoelectron backscattering on the nearest oxygen neighbors around Fe. The second weaker peak in the *R* range between 2.5 Å and 3.4 Å represents the contributions from more distant Fe coordination shells. Structural parameters of the local Fe neighborhood (type and average number of neighbors, radii and Debye–Waller factor of neighbor shells) were quantitatively resolved from the EXAFS spectrum by comparing the measured EXAFS signal with a model signal, constructed *ab initio* with the *FEFF6* program code (Rehr *et al.*, 1992) from the set of scattering paths of the photoelectron in a tentative spatial distribution of neighbor atoms. The model comprised six oxygen atoms at the same distance in the first coordination shell and two shells of iron neighbors and one shell of oxygen atoms at larger distances. The atomic species of neighbors are identified in the fit by their specific scattering factor and phase shift. Three variable parameters

Table 2

Parameters of the nearest coordination shells around Fe atoms in the FePd-EPS samples.

Average number of neighbor atoms (*N*), distance (*R*) and Debye–Waller factor (σ^2). The uncertainty of the last digit is given in parentheses. A best fit is obtained with the amplitude reduction factor $S_0^2 = 0.72$. The goodness-of-fit parameter, *R*-factor, is given in the last column.

Fe neighbor	<i>N</i>	<i>R</i> (Å)	σ^2 (Å ²)	<i>R</i> -factor
FePd-EPS(A)				
O	5.7 (6)	1.98 (2)	0.008 (1)	0.007
Fe	1.6 (6)	3.18 (3)	0.011 (9)	
Fe	4.5 (6)	3.45 (3)	0.011 (9)	
O	2.5 (5)	3.60 (2)	0.009 (1)	
FePd-EPS(B)				
O	5.7 (6)	1.99 (2)	0.008 (1)	0.011
Fe	0.3 (2)	3.11 (3)	0.007 (5)	
Fe	3.0 (6)	3.50 (3)	0.007 (5)	
O	1.9 (5)	3.64 (2)	0.005 (1)	

for each shell of neighbors are introduced in the model: the shell coordination number (*N*), the distance (*R*) and the Debye–Waller factor (σ^2). In addition, a common shift of the energy origin ΔE_0 is also allowed to vary. The amplitude-reduction factor S_0^2 is kept fixed at the value of 0.72 in agreement with previous Fe *K*-edge EXAFS analyses (Arçon *et al.*, 2012). A very good agreement between the model and the experimental spectra is found using the *k* range of 3.5 Å⁻¹ to 13.5 Å⁻¹ and *R* range of 1.0 Å to 3.5 Å (Fig. 7). A list of best-fit parameters is given in Table 2. In both samples, six oxygen atoms are identified in the first coordination shell at the same Fe–O distance of 1.98 Å, within error bars. In more distant coordination shells we found Fe and O atoms in both

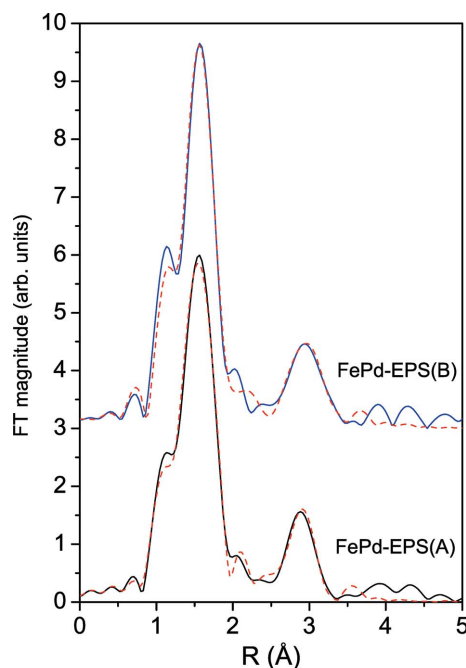


Figure 7 Fourier transform magnitude of k^3 -weighted Fe EXAFS spectra of FePd-EPS(A) and FePd-EPS(B) samples, calculated in the *k* range 3.5–13.5 Å⁻¹ and *R* range 1–3.5 Å. Experiment: solid line; best-fit EXAFS model: dashed line.

samples. There are six Fe atoms in the FePd-EPS(A) sample, two at a distance of 3.18 Å and four at 3.45 Å, while in the FePd-EPS(B) sample about three Fe atoms are identified, predominantly at the larger distance of 3.50 Å. In both samples about two oxygen atoms are located at a distance of about 3.6 Å. Fe *K*-edge EXAFS results suggest that iron in both FePd-EPS complexes is in a similar (but not identical) form, as in the Fe-EPS complex produced previously by *K. oxytoca* BAS-10 (Arčon *et al.*, 2012), or in ferritin (the iron storage protein). A comparison of the Fe EXAFS spectrum of the FePd-EPS samples with those of bulk crystalline iron oxides or hydroxides (Arčon *et al.*, 2005) clearly shows significant structural differences in the second coordination sphere of the local neighborhood of Fe in the sample. The coordination numbers of iron in the second coordination sphere are significantly smaller than in bulk iron oxides or hydroxides and the distribution of Fe neighbors is different.

Fe *K*-edge EXAFS results thus clearly indicate that iron in the sample is in the mineralized form of iron oxides/hydroxides. The coordination numbers, distribution of neighbor atoms, and large Debye–Waller factor in the second coordination shell show that the structure is not perfectly crystalline like in bulk iron oxides or hydroxides, but rather it is a mixture of different nano-crystalline iron oxides and hydroxides as in the previously reported Fe-EPS complex (Arčon *et al.*, 2012). Taking into account also Fe *K*-edge XANES results which show that iron is predominantly in the form of Fe³⁺, with a small amount of Fe²⁺ in the structure, the presence of a spinel structure as in Fe₃O₄ cannot be excluded. A direct coordination of iron oxide/hydroxides particles to a polysaccharide skeleton could not be detected with Fe *K*-edge EXAFS analysis. The main part of the iron atoms is located inside the oxide/hydroxides particles. Only iron atoms located on the surface of the nano-particles can form direct coordination with EPS. The relative amount of Fe atoms on the surface is very small compared with Fe atoms inside the nano-particle. Their contribution to the Fe EXAFS signal of the sample is below the detection limit. In Fe *K*-edge EXAFS analysis we also tested the presence of FePd intermetallic compounds. No Fe–Pd coordinations were detected, so we can exclude the presence of such intermetallic (Fe–Pd) compounds in both samples.

Fourier transforms of the Pd *K*-edge EXAFS spectra of the samples FePd-EPS(A), FePd-EPS(B) and Pd-EPS (Fig. 8) show typical local structure of metallic Pd. Comparison with the spectrum measured on Pd metal foil with f.c.c. crystal structure reveals the same pattern of neighbors up to about 5.5 Å. However, the height of individual neighbor peaks is lower than in the Pd foil, suggesting that the average number of neighbors is decreased and hence that clusters of Pd metal with f.c.c. crystalline structure are formed. From the observed reduction of the average number of neighbors, the size of the clusters can be deduced (Borowski, 1997; Frenkel, 1999; Arčon *et al.*, 2001). For quantitative Pd EXAFS analysis, the FEFF model is constructed, based on Pd metal with f.c.c. structure with lattice constant $a = 3.8900$ Å. Pd atoms are surrounded by 12 Pd atoms at 2.751 Å, 6 Pd at 3.890 Å, 24 Pd

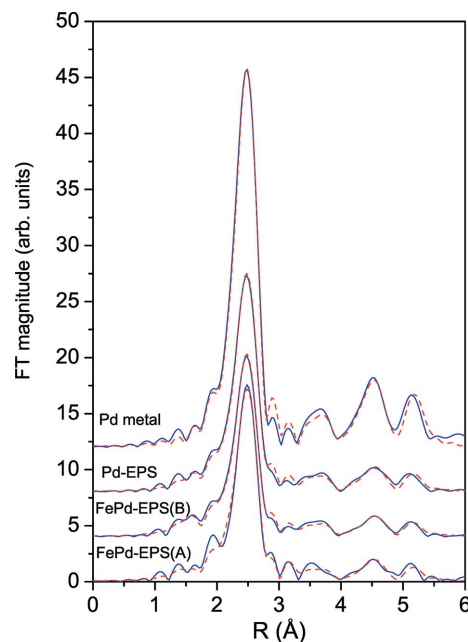


Figure 8

Fourier transform magnitude of k^3 -weighted Pd EXAFS spectra of Pd-EPS, FePd-EPS(A), FePd-EPS(B) samples and Pd metal with f.c.c. crystal structure, calculated in the k range 3–16 Å⁻¹ and R range 1–5.5 Å. Experiment: solid line; best-fit EXAFS model of the nearest coordination shells: dashed line.

at 4.764 Å and 12 Pd atoms at 5.501 Å. The contributions of the first four coordination shells in the R range from 1.0 Å to 5.5 Å (Fig. 8) is analyzed. The FEFF model comprised four single-scattering and all significant multiple-scattering paths from the nearest neighbor shells in Pd metal up to 5.6 Å. In addition, one Pd–O single scattering path is included in the model, to detect the eventual presence of oxygen neighbors in the first coordination shell around Pd, which can be expected, if (part of) Pd atoms form direct bonds to organic molecules (EPS) by Pd–O bridges.

The Pd metal foil spectrum is used to calibrate the model. A very good fit is obtained in the k range 3–16 Å⁻¹ and the R range 1–5.5 Å (Fig. 8), with just six variable parameters: the amplitude reduction factor S_0^2 (0.87 ± 0.03), shift of energy origin ΔE_0 (1.2 ± 0.5 eV), lattice expansion $\Delta r/r$ (0.002 ± 0.001), Debye temperature T_D (276 ± 20 K) in modeling the Debye–Waller factors of all paths, except the first, for which a separate Δr_1 (-0.008 ± 0.0015 Å) and Debye–Waller factor σ_1^2 (0.0071 ± 0.0002 Å²) are introduced. The shell coordination numbers are fixed at their f.c.c. values. As expected, no oxygen neighbors were detected in the first coordination shell of Pd in the metal foil.

In modeling the Pd EXAFS spectra of the three samples FePd-EPS(A), FePd-EPS(B) and Pd-EPS, the same model parameters were varied, except that the amplitude reduction factor S_0^2 is kept fixed at the value of Pd metal foil, while the number of Pd neighbors in the first four coordination shells of the f.c.c. lattice are allowed to vary. Three variable parameters (distance, Debye–Waller factor and coordination number) are used to model the contribution of oxygen neighbors. Very good fits were obtained in the same k and R range as for the

Table 3

Parameters of the nearest coordination shells around Pd atoms in the FePd-EPS samples and in Pd metal with f.c.c. crystal structure ($a = 3.8900 \text{ \AA}$).

Average number of neighbor atoms (N), distance (R) and Debye–Waller factor (σ^2). The uncertainty of the last digit is given in parentheses. A best fit is obtained with the amplitude reduction factor $S_0^2 = 0.87$ (5). The goodness-of-fit parameter, R -factor, is given in the last column.

Pd neighbor	N	R (\AA)	σ^2 (\AA^2)	R -factor
FePd-EPS(A)				
O	0.4 (2)	1.95 (3)	0.005 (2)	0.014
Pd	7.6 (5)	2.749 (2)	0.0069 (3)	
FePd-EPS(B)				
O	0.7 (2)	1.99 (3)	0.005 (2)	0.005
Pd	7.6 (3)	2.741 (2)	0.0071 (2)	
Pd-EPS				
O	0.5 (2)	1.99 (3)	0.005 (2)	0.004
Pd	8.8 (4)	2.742 (2)	0.0071 (2)	
Pd metal				
Pd	12	2.745 (2)	0.0058 (2)	0.003

Pd metal foil spectrum (Fig. 8). Best-fit parameters of the nearest coordination shells are listed in Table 3. In all three samples, Pd neighbors in the first four coordination shells of the f.c.c. structure are found at the same distance (within error bars) and the same or slightly larger Debye–Waller factors as in the Pd metal foil, but the average coordination numbers are lower than in the bulk Pd metal. The average coordination number of Pd neighbors in the first coordination shell is between 60% and 70% of the value in the bulk f.c.c. metal, while in the next three more distant coordination shells the average number of neighbors is even lower (between 40% and 50% of the value in the bulk f.c.c. metal), indicating that nanoparticles with f.c.c. structure of Pd metal are formed. The average sizes of the nanoparticles can be deduced from the observed reduction of the average number of neighbors. Using the method described previously (Arçon *et al.*, 2001), we can estimate that the average size of Pd metal nanoparticles is between 1.0 nm and 1.5 nm. In all three samples we found that Pd atoms have on average from 0.4 to 0.7 oxygen neighbors at the short distance characteristic for the Pd–O covalent bond. The result indicates that the Pd atoms on the surface of the Pd metallic nanoparticles are bonded to the organic phase (EPS) or organic phosphate forming Pd–O bridges.

3.4. Iron, palladium and phosphorous distribution in biomaterials

Distribution maps of Fe, Pd and P, recorded by μ -XRF in a randomly chosen $100 \mu\text{m} \times 100 \mu\text{m}$ area of FePd-EPS(A) and FePd-EPS(B) homogeneous sample pellets with $1 \mu\text{m}$ lateral resolution, are shown in Figs. 9 and 10. Fe and Pd are found agglomerated in meter-size particles or clusters and they are not randomly mixed within individual particles, but they are spatially separated. It is possible to observe islands of Pd-containing particles randomly distributed on Fe-containing

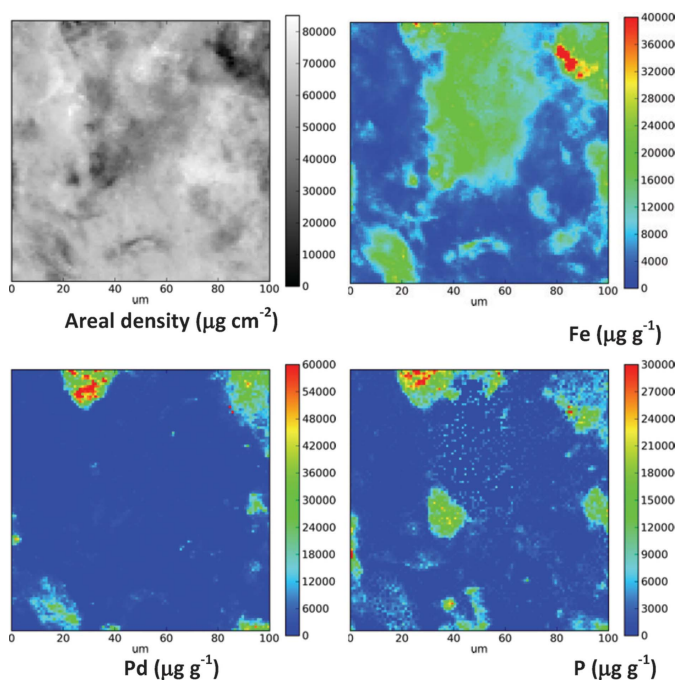


Figure 9
Areal density of the sample, iron (Fe), palladium (Pd) and phosphorus (P) quantitative SR μ -XRF distribution maps recorded in the FePd-EPS(A) sample pellets at an excitation energy of 7300 eV. The areal density (top, left) was calculated from the absorption of X-rays at 7300 eV, taking into account the absorption coefficient in carbohydrates at 7300 eV. Scan size is $100 \mu\text{m} \times 100 \mu\text{m}$.

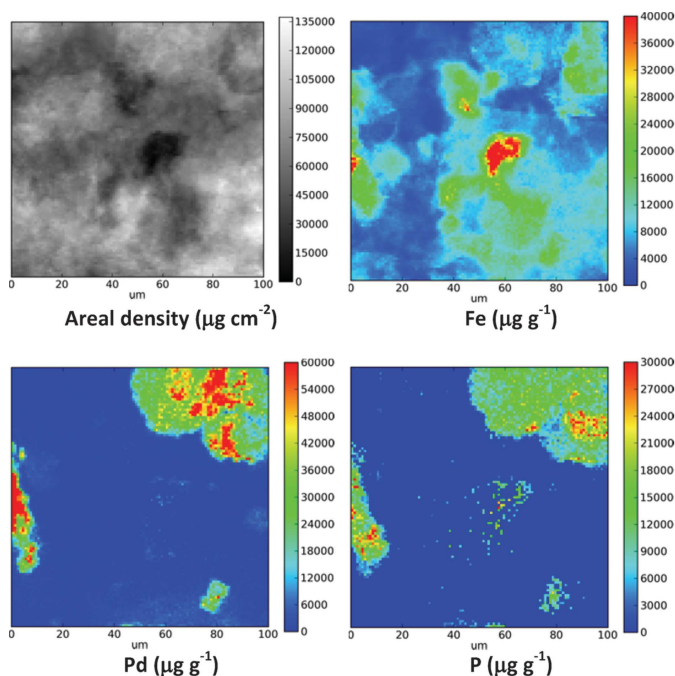


Figure 10
Areal density of the sample, iron (Fe), palladium (Pd) and phosphorus (P) quantitative SR μ -XRF distribution maps recorded in the FePd-EPS(B) sample pellets at an excitation energy of 7300 eV. The areal density (top, left) was calculated from the absorption of X-rays at 7300 eV, taking into account the absorption coefficient in carbohydrates at 7300 eV. Scan size is $100 \mu\text{m} \times 100 \mu\text{m}$.

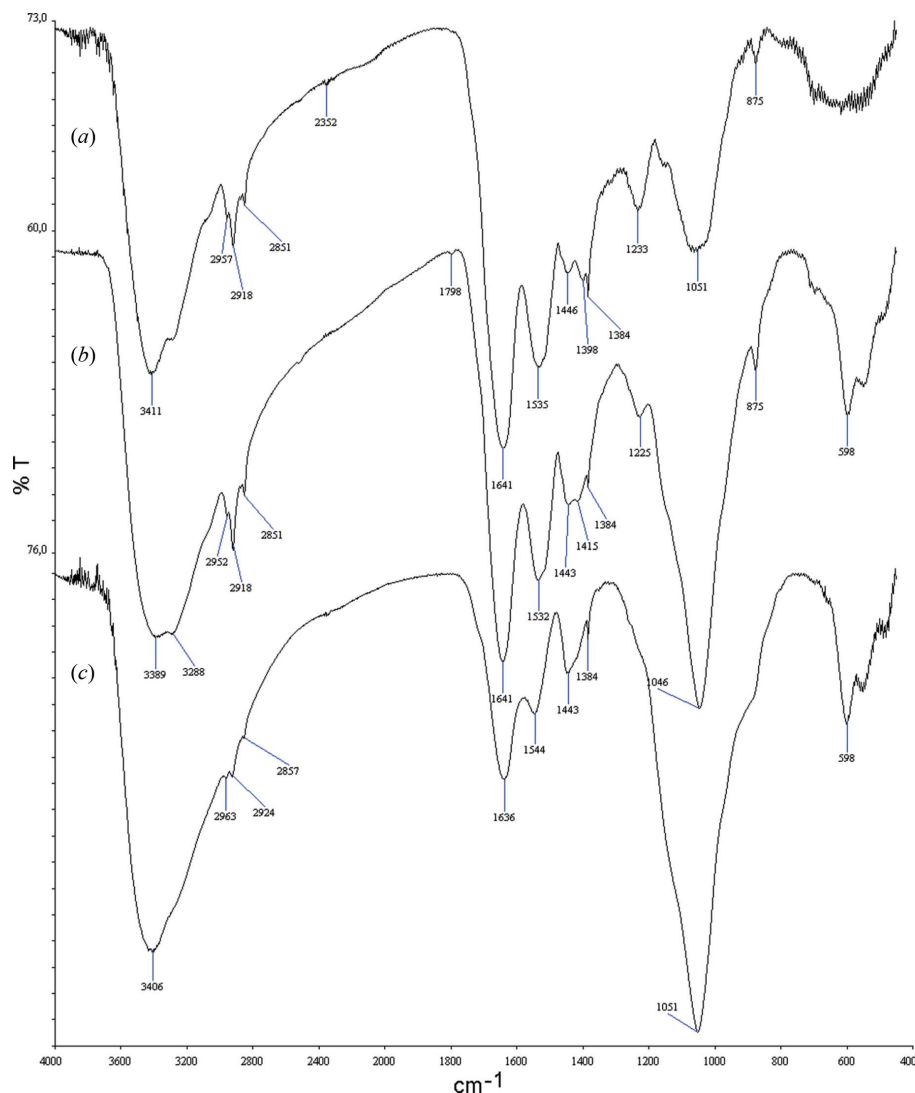


Figure 11
FTIR spectra of (a) Pd-EPS, (b) FePd1-EPS(A) and (c) FePd2-EPS(B). The absorbance peak of organic phosphate is at 1051 cm^{-1} .

particles. Phosphorous is co-localized mainly with Pd distribution.

3.5. FTIR

FTIR analysis is used to confirm this evidence and changes in EPS matrices after addition of metal cations. The measured FTIR spectra are shown in Fig. 11. A peak at 1051 cm^{-1} , characteristic of organic phosphates (George *et al.*, 1994), is observed in all spectra, but mainly in FePd-EPS(A) and FePd-

EPS(B) samples. The phosphate peak area increases proportionally with total iron amount in the EPS.

3.6. Test of catalytic activity of FePd-EPS(B)

The catalytic activity of Pd-EPS, FePd-EPS(A) and FePd-EPS(B) was tested in the hydrodechlorination of 1,2,4-trichlorobenzene (I). Dry complexes were rehydrated in distilled water for about 10 min and the aqueous suspension used as catalyst in the hydrodechlorination reaction (Fig. 12).

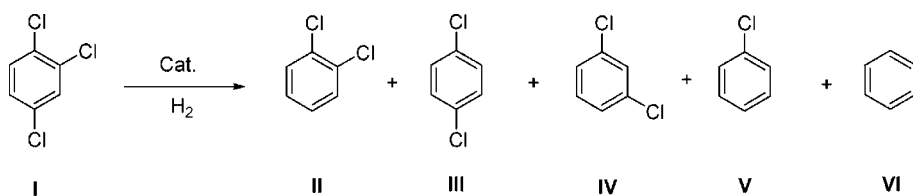


Figure 12
The hydrodechlorination reaction of 1,2,4-trichlorobenzene.

The hydrodechlorination experiment with FePd-EPS(B) was at first carried out at 333 K and 3 MPa of H_2 for 20 h and using a substrate/Pd molar ratio of 61/1; a low substrate conversion was obtained and 1,2-dichlorobenzene (II) was the main product (15%), while the other dichloro isomers III and IV and both chlorobenzene (V) and benzene (VI) were formed in negligible amounts

Table 4

Hydrogenation of 1,2,4-trichlorobenzene (I).

Reaction conditions: substrate = 0.24 mmol; H₂O = 2 ml; THF = 1 ml.

Run	Catalyst	I/Pd catalyst molar ratio	Conversion (%)	II yield (%)	III yield (%)	IV yield (%)	V yield (%)	VI yield (%)
1	FePd-EPS(B)	61	23	15	3	3	1	1
2	FePd-EPS(B)	8	100	–	–	–	–	100
3†	FePd-EPS(B)	8	100	42	12	6	20	20
4	FePd-EPS(A)	8	90	34	9	6	21	20
5†	FePd-EPS(A)	8	89	23	4	3	15	44
6	Pd-EPS	8	76	36	6	6	19	9
7†	Pd-EPS	8	84	42	17	11	9	5

† Experiment carried out using the catalytic phase, recovered from the previous run.

(Table 4, Run 1). In order to improve the conversion we carried out an experiment adopting the same reaction conditions but with an increased catalyst amount (substrate/Pd molar ratio = 8/1). In this case a complete conversion was achieved, and benzene (VI) was the only product (Table 4, Run 2). Note that the aqueous catalytic phase was recovered and reused in a consecutive experiment by adding fresh 1,2,4-trichlorobenzene. Again the conversion was complete but we observed a partial loss of the hydrodechlorination efficiency of the catalyst: now benzene was formed only for 20% and the main product was 1,2-dichlorobenzene (II) (Table 4, Run 3). The behavior of the catalyst FePd-EPS(A) was less efficient than fresh FePd-EPS(B) and similar to that of the corresponding recycled FePd-EPS(B) catalyst; it is, however, interesting to note the significant increase in the amount of benzene working at 353 K instead of 333 K (Table 4, Runs 4 and 5). The catalytic activity of both FePd-EPS, especially that of fresh FePd-EPS(B), was higher than Pd-EPS used (Table 4, Runs 6 and 7).

4. Discussion

In previous reports (Baldi *et al.*, 2001, 2009; Leone *et al.*, 2007) it was demonstrated that the strain BAS-10 produces, under anaerobic conditions, a specific EPS during citrate fermentation. *K. oxytoca* BAS-10 secretes this specific EPS, which can be considered a modified colanic acid. Colanic acid structures are different and are present in many Gram-negative bacteria (Chen *et al.*, 1987; Withfield, 2006), but this analogue is special because it binds to many metals (Arčon *et al.*, 2012) as a result of environmental adaptation typical of acid mine drainage.

To date, only monometallic EPS have been bio-generated (Baldi *et al.*, 2010, 2011; Paganelli *et al.*, 2013). In this study we produced for the first time two bi-metallic EPS species in order to obtain more biomaterials from the microbial cultures. Indeed, yields of FePd-EPS(A) and FePd-EPS(B) were significantly higher than the yield of Pd-EPS obtained without iron addition (Table 1). This is due to the fact that Fe(III) is a nutrient for *K. oxytoca* BAS-10 (Gallo *et al.*, 2012), whereas Pd(II) is an inhibitor. Furthermore, the relative amount of Pd incorporated in the EPS during the fermentation is much higher in the presence of iron than in the absence of iron. Also iron recovery in Me-EPS was higher when the weight of Fe

and Pd salts was the same [67% in FePd-EPS(A) versus 55% in FePd-EPS(B)].

Another significant difference was found in the morphology between mono- and bi-metal EPS. In both cases electron-dense nano-particles of Pd, or Fe and Pd embedded in EPS, are formed, but with significant differences in particle size (Fig. 2). In the presence of iron, larger particles containing both metals (Fe and Pd) are produced. The metal EPS tends to increase in size due to a helix-coil conformation typical of ionic polysaccharides (Nilsson & Piculell, 1991). This ionic characteristic of EPS increases due to the EPS phosphorylation induced by the presence of Fe(III) in the culture medium. From two-dimensional distribution maps of Fe, Pd and P, obtained by micro-XRF analysis (Figs. 9 and 10), it is evident that Fe and Pd are not randomly mixed within individual particles; they are instead spatially separated. Pd-containing particles are randomly distributed on Fe-containing particles. Interestingly, phosphorous, present in the form of organic phosphates, as shown by FTIR analysis, is co-localized mainly with Pd particles. The results indicate that the coordination of EPS with Pd particles is most probably mediated by phosphoric ester groups bonded to EPS.

In many bacteria and therefore also in the *Klebsiella* genus, organic and inorganic phosphates are modulated by tyrosine kinase and a low-molecular-weight phosphatase, which are in the inner membrane and periplasmic space (Vincent *et al.*, 2000; Grangeasse *et al.*, 2007). In the presence of high metal concentrations, the phosphorylation activity can be considered a further mechanism of metal resistance (Macaskie, 2007).

Fe and Pd *K*-edge EXAFS and XANES analysis revealed the chemical state of the two metals in the Pd-EPS and FePd-EPS complexes. The results clearly indicate that iron is in both FePd-EPS samples in the mineralized form of iron oxides/hydroxides, predominantly in the form of Fe³⁺, with a small amount of Fe²⁺ in the structure, most probably a mixture of different nano-crystalline iron oxides and hydroxides, as in the previously reported Fe-EPS complex (Arčon *et al.*, 2012). Palladium, on the other hand, is in all three samples present predominantly as Pd(0) metal, in the form of nanoparticles with f.c.c. crystal structure. The average size of Pd metal nanoparticles is of the order of a few nanometers. In all three samples a smaller amount of Pd atoms, most probably those on the surface of metallic nanoparticles, is bound to oxygen by a

Pd–O covalent bond. Taking into account also micro-XRF and FTIR analysis we can conclude that the Pd metallic nanoparticles are bonded to the EPS *via* the Pd–O–P bridges on the phosphates.

The large extent of reduction of Pd(II) to Pd(0) is probably due to strain BAS-10 metabolism under anaerobic conditions; when an excess of acetic acid is formed, pyruvate is converted into formic acid, with a certain reducing power, by pyruvate formate lyase (Gallo *et al.*, 2012), but we cannot exclude a role of the iron species. The influence of iron on the catalytic properties of palladium species on reactivity, selectivity and the possibility to recycle is tested. In all cases the recycle was possible but a partial deactivation was observed, even if lower than that found by us with commercial heterogeneous palladium catalysts (data not shown) in aqueous reaction medium under the same experimental conditions. We could explain this partial deactivation by hypothesizing a poisoning of the palladium surface and/or a change of the structure of the recycled catalyst with respect to the pristine one. The increase in size of metal particles, as shown by TEM analyses, could also play a role. The catalytic activity of both FePd-EPS, especially that of fresh FePd-EPS(B), was higher than Pd-EPS used, so indicating the positive and synergic role of the ferric species to favor the hydro-breaking of the Ar–Cl bond. A further advantage of these new bimetallic catalysts is related to their preparation, that is faster than the production of Pd-EPS only, with higher yield per liter and better recovery of both metals in the EPS framework (Table 1).

5. Conclusion

The addition of Fe(III) as ferric citrate to an anaerobic culture of *K. oxytoca* BAS-10 significantly increases the EPS secretion in the presence of palladium species and permits their higher incorporation in the polysaccharide framework. The specific branched EPS, with a modified structure with respect to other colanic acids, typical of *Enterobacteriaceae*, is able to embed iron oxides and metallic Pd(0), producing nanoparticles of different size. A detailed investigation with different analytical, spectroscopic and microscopic techniques has permitted a better view of this complex structure, showing the absence of any Pd–Fe bonds or Fe–O–Pd bridges. The distribution of phosphorous species, which are co-localized with palladium, might indicate that the coordination of EPS with metallic Pd particles is mediated by phosphoric ester groups. Finally, a new bimetallic FePd-EPS complex showed improved catalytic properties in the hydrodechlorination process of an aromatic polychloro model compound.

Acknowledgements

This research was supported by the Slovenian Research Agency (P1-0112) by DESY and the European Community Seventh Framework Programme (FP7/2007-2013) under the CALIPSO grant agreement, No. 312284 (EU Support of Access to Synchrotrons/FELs in Europe). Access to the synchrotron radiation facilities at ESRF (beamline ID21,

project LS-2225), HASYLAB at DESY (beamline C) in Hamburg (project I-20110511 EC) and ELETTRA (beamline XAFS, project 20115112) is acknowledged. We would like to thank Hiram Castillo-Michel of ESRF, Roman Chernikov and Edmund Welter of HASYLAB, and Giuliana Aquilanti and Luca Olivi of ELETTRA for support and expert advice on beamline operation.

References

- Arçon, I., Kolar, J., Kodre, A., Hanžel, D. & Strlič, M. (2007). *X-ray Spectrom.* **36**, 199–205.
- Arçon, I., Mozetič, M. & Kodre, A. (2005). *Vacuum*, **80**, 178–183.
- Arçon, I., Piccolo, O., Paganelli, S. & Baldi, F. (2012). *Biometals*, **25**, 875–881.
- Arçon, I., Tuel, A., Kodre, A., Martin, G. & Barbier, A. (2001). *J. Synchrotron Rad.* **8**, 575–577.
- Baldi, F., Marchetto, D., Battistel, D., Daniele, S., Faleri, C., De Castro, C. & Lanzetta, R. (2009). *J. Appl. Microbiol.* **107**, 1241–1250.
- Baldi, F., Marchetto, D., Paganelli, S. & Piccolo, O. (2011). *New Biotechnol.* **29**, 74–78.
- Baldi, F., Marchetto, D., Zanchettin, D., Sartorato, E., Paganelli, S. & Piccolo, O. (2010). *Green Chem.* **12**, 1405–1409.
- Baldi, F., Minacci, A., Pepi, M. & Scozzafava, A. (2001). *FEMS Microbiol. Ecol.* **36**, 169–174.
- Battistel, D., Baldi, F., Gallo, M., Faleri, C. & Daniele, S. (2015). *Talanta*, **132**, 294–300.
- Borowski, M. (1997). *J. Phys. IV Fr.* **7(C2)**, 259–260.
- Chen, Y. M., Tobin, J. F., Zhu, Y., Schleif, R. F. & Lin, E. C. C. (1987). *J. Bacteriol.* **169**, 3712–3719.
- Coe, E. M., Bowen, L. H., Speer, J. A., Wang, Z., Sayers, D. E. & Bereman, R. D. (1995). *J. Inorg. Biochem.* **58**, 269–278.
- Deschatre, M., Ghillebaert, F., Guezennec, J. & Colin, C. S. (2013). *Appl. Biochem. Biotechnol.* **171**, 1313–1327.
- Dominko, R., Sirisopanaporn, C., Masquelier, C., Hanžel, D., Arçon, I. & Gabersček, M. (2010). *J. Electrochem. Soc.* **157**, A1309–A1316.
- Elam, W., Ravel, B. D. & Sieber, J. R. (2002). *Radiat. Phys. Chem.* **63**, 121–128.
- Frenkel, A. I. (1999). *J. Synchrotron Rad.* **6**, 293–295.
- Gallo, G., Baldi, F., Renzone, G., Gallo, M., Cordaro, A., Scaloni, A. & Puglia, A. (2012). *Microb. Cell Fact.* **11**, 152–167.
- George, L., Sankaran, K., Viswanathan, K. S. & Mathews, C. K. (1994). *Appl. Spectrosc.* **48**, 7–12.
- Grangeasse, C., Cozzone, A. J., Deutscher, J. & Mijakovic, I. (2007). *Trends Biochem. Sci.* **32**, 86–94.
- He, F. & Van Espen, P. J. (1991). *Anal. Chem.* **63**, 2237–2244.
- Koren, Š., Arçon, I., Kump, P., Nečemer, M. & Vogel-Mikuš, K. (2013). *Plant Soil*, **370**, 125–148.
- Kuzma, M., Dominko, R., Hanžel, D., Kodre, A., Arçon, I., Meden, A. & Gabersček, M. (2009). *J. Electrochem. Soc.* **156**, A809–A816.
- Kump, P., Nečemer, M., Vogel-Mikuš, K., Rupnik, Z., Ponikvar, D., Pelicon, P., Pongrac, P., Simčič, J. & Budnar, M. (2007). *Vienna, 16–20 April (IAEA/AL/181)*. IAEA, Vienna, Austria, pp. 91–95.
- Leone, S., De Castro, C., Parrilli, M., Baldi, F. & Lanzetta, R. (2007). *Eur. J. Org. Chem.* **2007**, 5183–5189.
- Macaskie, L. (2007). *Chem. Technol. Biotech.* **49**, 357–379.
- Nilsson, S. & Piculell, L. (1991). *Macromolecules*, **24**, 3804–3811.
- Paganelli, S., Piccolo, O., Baldi, F., Tassini, R., Gallo, M. & La Sorella, G. (2013). *Appl. Catal. Gen.* **451**, 144–152.
- Perrin, D. D. & Armarego, W. L. F. (1988). *Purification of Laboratory Chemicals*. Oxford: Pergamon Press.
- Ravel, B. & Newville, M. (2005). *J. Synchrotron Rad.* **12**, 537–541.
- Rehr, J. J., Albers, R. C. & Zabinsky, S. I. (1992). *Phys. Rev. Lett.* **69**, 3397–3400.

- Rigo, C., Zamego, L., Rampazzo, G. & Argese, E. (2009). *Chemosphere*, **77**, 510–517.
- Sherman, J. (1955). *Spectrochim. Acta*, **7**, 283–306.
- Shuhong, Y., Meiping, Z., Hong, Y., Han, W., Shan, X., Yan, L. & Jihui, W. (2014). *Carbohydr. Polym.* **101**, 50–56.
- Solé, V. A., Papillon, E., Cotte, M., Walter, P. & Susini, J. (2007). *At. Spectrosc.* **62**, 63–68.
- Vincent, C., Duclos, B., Grangeasse, C., Vaganay, E., Riberty, M., Cozzone, A. J. & Doublet, P. (2000). *J. Mol. Biol.* **304**, 311–321.
- Watt, R. K. (2011). *Biometals*, **24**, 489–500.
- Withfield, C. (2006). *Annu. Rev. Biochem.* **75**, 39–98.
- Wong, J., Lytle, F. W., Messmer, R. P. & Maylotte, D. H. (1984). *Phys. Rev. B*, **30**, 5596–5610.